CrossMark

ORIGINAL PAPER

Experimental determination of liquidus H₂O contents of haplogranite at deep-crustal conditions

A. R. Makhluf[1] · R. C. Newton[1] · C. E. Manning[1]

Abstract The liquidus water content of a haplogranite melt at high pressure (P) and temperature (T) is important, because it is a key parameter for constraining the volume of granite that could be produced by melting of the deep crust. Previous estimates based on melting experiments at low P ($\leq$0.5 GPa) show substantial scatter when extrapolated to deep crustal P and T (700–1000 °C, 0.6–1.5 GPa). To improve the high-P constraints on H₂O concentration at the granite liquidus, we performed experiments in a piston–cylinder apparatus at 1.0 GPa using a range of haplogranite compositions in the albite (Ab: $NaAlSi_3O_8$)—orthoclase (Or: $KAlSi_3O_8$)—quartz (Qz: SiO_2)—H₂O system. We used equal weight fractions of the feldspar components and varied the Qz between 20 and 30 wt%. In each experiment, synthetic granitic composition glass + H₂O was homogenized well above the liquidus T, and T was lowered by increments until quartz and alkali feldspar crystalized from the liquid. To establish reversed equilibrium, we crystallized the homogenized melt at the lower T and then raised T until we found that the crystalline phases were completely resorbed into the liquid. The reversed liquidus minimum temperatures at 3.0, 4.1, 5.8, 8.0, and 12.0 wt% H₂O are 935–985, 875–900, 775–800, 725–775, and 650–675 °C, respectively.

Quenched charges were analyzed by petrographic microscope, scanning electron microscope (SEM), X-ray diffraction (XRD), and electron microprobe analysis (EMPA). The equation for the reversed haplogranite liquidus minimum curve for $Ab_{36.25}Or_{36.25}Qz_{27.5}$ (wt% basis) at 1.0 GPa is $T = -0.0995w_{H_2O}^3 + 5.0242w_{H_2O}^2 - 88.183w_{H_2O} + 1171.0$ for $0 \leq w_{H_2O} \leq 17$ wt% and T is in °C. We present a revised $P - T$ diagram of liquidus minimum H₂O isopleths which integrates data from previous determinations of vapor-saturated melting and the lower pressure vapor-undersaturated melting studies conducted by other workers on the haplogranite system. For lower H₂O (<5.8 wt%) and higher temperature, our results plot on the high end of the extrapolated water contents at liquidus minima when compared to the previous estimates. As a consequence, amounts of metaluminous granites that can be produced from lower crustal biotite–amphibole gneisses by dehydration melting are more restricted than previously thought.

Keywords Haplogranite · Granite · Liquidus · Cotectic · Dehydration melting · Feldspar · Magma · H₂O · Water · Granophyre · Graphic granite · Experimental petrology

Communicated by Mark S Ghiorso.

✉ A. R. Makhluf
amakhluf@epss.ucla.edu

1 Department of Earth, Planetary and Space Sciences, University of California, Los Angeles, 595 Charles E. Young Drive, East, 1679 Geology Building, Los Angeles, CA 90095-1567, USA

Introduction

Many granites are derived from melting of the lower crust (Brown and Fyfe 1970; Brown 2001, 2007). A key control on the degree of crustal melting is the dependence of the melting temperature at any pressure on the liquidus H₂O content of granitic magmas. Phase relations in the simple granite system—i.e., haplogranite, with the anhydrous ternary components albite (Ab: $NaAlSi_3O_8$), orthoclase (Or: $KAlSi_3O_8$), and quartz (Qz: SiO_2)—are well known to high

🖄 Springer

pressure at H_2O saturation (Tuttle and Bowen 1958; Burnham and Jahns 1962; Luth et al. 1964; Boettcher and Wyllie 1968; Seck 1971; Huang and Wyllie 1975). However, the increasingly sodic and silica-poor minimum melt composition with rising pressure (Tuttle and Bowen 1958; Luth et al. 1964; Luth 1976) makes melting in the presence of pure H_2O an unlikely scenario for the generation of granitic liquids. In contrast, decrease of H_2O activity, either by the absence of a free aqueous phase or by dilution of the fluid with another component, yields minimum melts with more typical primary granite compositions (Pichavant 1987; Ebadi and Johannes 1991; Holtz et al. 1992; Aranovich et al. 2013). These conclusions support a general model of granite production by crustal melting at low H_2O activity.

To understand the links between melting temperature, H_2O concentration, and melt volume at deep-crustal conditions, it is necessary to know the concentration of dissolved H_2O on the liquidus at high pressure. However, previous studies of the haplogranite liquidus at reduced H_2O activity and 1.0 GPa (Keppler 1989; Ebadi and Johannes 1991; Aranovich et al. 2013) do not report melt H_2O concentrations. Holtz et al. (2001a) determined the liquidus minimum temperature in this system at 1 wt% H_2O at 0.8 GPa. In the absence of direct determinations at lower crustal pressures, the liquidus H_2O content must be estimated based on extrapolation of low-P experimental data (Johannes 1985; Johannes and Holtz 1991; Holtz et al. 2001a) or calculated from thermodynamic models (e.g., Holland and Powell 2001).

Testing such extrapolations is made difficult by the fact that extraordinary steps must be taken to demonstrate equilibrium in experiments in granitic systems. The H_2O undersaturated liquidus is subject to considerable error in the conventional melting experiments because of analytical errors in measuring the H_2O content of quenched glasses, the difficulty in homogenizing crystalline or glass starting materials into the melt, supercooling of granitic melts and metastable crystalline phases forming from a supercooled liquid, and the sluggish kinetics in both the formation of metastable crystalline phases as well as the approach to equilibrium assemblages (Paillat et al. 1992). Ideally, chemical equilibrium should be defined by reversal experiments in which an equilibrium final state is approached from both crystal-undersaturated and saturated directions, with phase assemblages and compositions approaching common values. These are criteria that can be very hard to realize in charges of low H_2O content in quartzofeldspathic systems, even for experiments at high temperature and for long duration (Holtz et al. 2001a).

Here, we describe experiments which provide the first experimental constraints on H_2O concentration at the minimum or eutectic (below we use "minimum" for brevity) in the haplogranite–H_2O system at pressures relevant to lower crustal melting (1.0 GPa). Problems with nucleation in undercooled liquids required a two-step experimental sequence to establish equilibrium. The constraints on water concentration along the granite liquidus were obtained over a range of H_2O concentrations and granite compositions in the anhydrous Ab–Or–Qz ternary. The experiments establish the temperature dependence of the equilibrium H_2O contents for haplogranite minimum melts.

Methods

Compositional considerations

Experiments in the haplogranite–H_2O system are complicated by two main factors: (1) at any given bulk H_2O content, a range of compositions must be explored to identify the one which produces 100% liquid at the lowest temperature and (2) reaction rates involving feldspar, quartz, and liquid can be quite sluggish, especially at low temperatures and low H_2O activities. As will become clear below, explicitly addressing both these issues in a single study would involve a vast number of experiments. Accordingly, we designed the present investigation so as to minimize the compositional space which needed to be explored while ensuring that the results reflect equilibrium.

Previous work at reduced H_2O activity provides a guide to the optimal compositional range at 1.0 GPa. Johannes and Holtz (1996) present summary diagrams showing the liquidus surfaces in the haplogranite ternary at a range of pressures and H_2O activities. Inspection of these ternaries reveals two key points. First, the liquidus temperatures increase relatively slowly away from the ternary minimum. That is, dT/dX, where X is composition, is shallow near the minimum, and small changes of 10–20 °C yield relatively large changes in the liquidus melt composition. Second, even in the best cases, the minima are only constrained to within 5–10 wt% of the anhydrous components. Figure 1 illustrates this point using 1.0 GPa results from Ebadi and Johannes (1991). The minimum compositions Fig. 1, are shown in filled circles; however, the bounds for the possible location of the minima as constrained by bracketing experiments are shown with the shaded boxes. Ebadi and Johannes (1991) concluded that the concentration of the Or component in minimum melts increases with decreasing H_2O activity. Though probably true, the change could be greater or less than suggested, because uncertainties in the true minimum composition at any given H_2O activity are quite large. Similarly, at 0.2–1.0 GPa and a range of H_2O activities, reported Qz content at the liquidus minimum ranges shows no systematic variation with H_2O activity (Pichavant 1987; Ebadi and Johannes 1991; Holtz et al. 1992, 2001b; Aranovich et al. 2013). These relatively large uncertainties in minimum
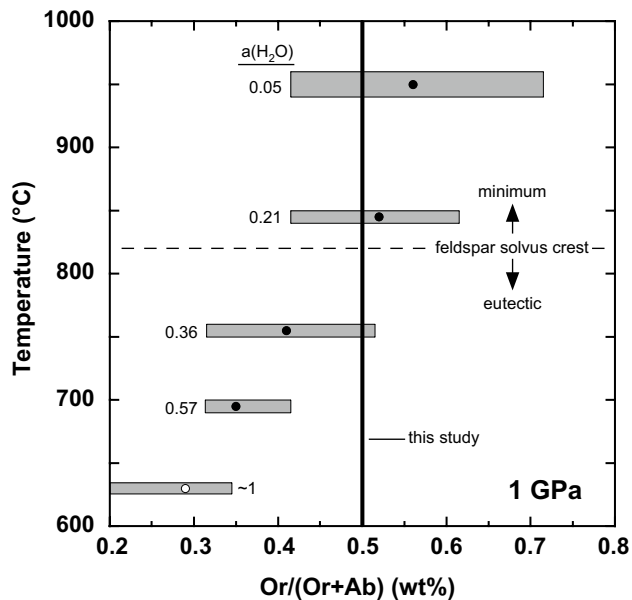
Fig. 1 Variation in liquidus Or/(Or + Ab), in wt%, of haplogranite melts with temperature and H_2O activity. *Open circle*, datum of Luth et al. (1964) at H_2O saturation, or H_2O activity (a_{H_2O}) of ~1 (approximate because aqueous solutes lower a_{H_2O} somewhat); *filled circles*, data of Ebadi and Johannes (1991). *Gray rectangles* indicate temperature and compositional uncertainties, as inferred from Fig. 3 of Luth et al. (1964) and Fig. 6 of Ebadi and Johannes (1991). While there is a trend to higher Or with decreasing a_{H_2O}, the compositional uncertainties are quite large. The present study was conducted at a_{H_2O} <1 and fixed Or content of 50 wt% (*vertical line*, see text). Also shown for reference is the location of the crest of the alkali feldspar solvus at 1 GPa (Morse 1970). Below ~820 °C, the haplogranite system displays eutectic melting behavior, whereas above the system melts at a ternary minimum on the feldspar–quartz cotectic (e.g., Johannes and Holtz 1996)

melt compositions at H_2O-undersaturated conditions likely reflect, at least in part, the shallow dT/dX of liquidus surfaces near the minima.

In the present study, we used a single, fixed Or/(Or + Ab) ratio of 50 wt% (Fig. 1). Three observations support this simplification. First, within uncertainty, this composition overlaps with that of the minimum melt over a range of H_2O activities, but most importantly at lower H_2O activity relevant for crustal melting. Second, at these H_2O activities and even at higher values, where Or_{50} is probably more potassic than the minimum, the liquidus minimum temperature at Or_{50} is likely no more than 10–20 °C higher than minimum melting due to low dT/dX of liquidus surfaces. This is comparable to the best expected uncertainty in our reversal brackets (see below). Finally, the crest of the alkali feldspar solvus is ~820 °C at 1.0 GPa, but at Or_{50} bulk composition, even experiments at subsolvus temperature can be expected to produce a single potassic feldspar due to the strong K partitioning relative to the liquid (e.g., Ebadi and Johannes 1991). Thus, by adopting this simplification

of a bulk composition with fixed Or/(Or+Ab) = 0.5, we can obtain comparatively tight constraints on the liquidus minimum temperature, even though the experimental liquid composition may differ slightly from the true minimum melt at the highest H_2O activities associated with wet melting. Notably, Ebadi and Johannes (1991) report that the feldspar K:Na weight ratio of the dry solidus at 1.0 GPa is close to 1:1, and Or_{50} is close to Or_{47} investigated by Holtz et al. (2001a) at 0.8 GPa at 1 wt% H_2O.

Fixing the Or/Ab ratio allowed evaluation of two other compositional variables. The role of Qz content was explored by adding variable amounts of Qz to anhydrous compositions with equal Ab and Or masses. Thus, the Qz content uniquely defines each anhydrous bulk composition through Ab = Or = (100 − Qz)/2 on a wt% basis. We conducted experiments on anhydrous bulk compositions with 25, 27.5, and 30 wt% Qz (several exploratory experiments were conducted at 20 wt% Qz).

Finally, liquidus minimum temperatures were investigated at five different target water contents: 3.0, 4.1, 5.8, 8.0, and 12.0 wt% H_2O. These H_2O contents were chosen to cover a wide range of compositions between dry and H_2O-saturated liquids. The H_2O content at the vapor-saturated solidus is 17.0 ± 1 wt% H_2O (Luth et al. 1964; Luth 1976). Melting temperature at H_2O saturation is subject to some uncertainty. Luth (1976) summarized results of Luth et al. (1964) as indicating minimum melting at 630 ± 5 °C. However, he noted that data from subsequent workers argued for a downward revision by 10–15 °C. Nevertheless, later work typically uses the uncorrected temperature of Luth et al. (1964). For example, Ebadi and Johannes (1991) and Johannes and Holtz (1991) use 635 °C for the H_2O-saturated haplogranite solidus. We use this value in the present study to facilitate comparison with the extensive body of work of Johannes, Holtz, and coworkers.

Starting materials

Starting materials were synthetic $NaAlSi_3O_8$ glass (made following Hayden and Manning 2011), synthetic sanidine glass (prepared by D. B. Stewart, # X95GQA[1]), and Puratronic SiO_2 glass. Anhydrous starting bulk compositions were generated from the three glass end members and then finely ground under acetone in an agate mortar. The ground glass mixtures were baked at 600 °C to remove any organic residue, packed and sealed into platinum capsules, and then fused in a one atmosphere tube furnace at 1400 °C for ~3 h. The liquid was quenched in air to a glass. The glass was again fine-ground under acetone in an agate mortar and baked at 600 °C. The resulting glasses contained minor SiO_2-rich patches (see below).

For the high-*P* experiments, Pt tube segments of either 2.0 or 3.5-mm diameter were welded at one end and

annealed using an oxy-acetylene torch. A dry glass powder was weighed into the capsule and then ultra-pure 18-MΩ-cm water was added with a microliter syringe in slight excess of the amount intended. The water was allowed to evaporate on the balance until the desired weight was reached. The capsule was then pinched and sealed by arc welding. Weight loss upon sealing was on average 160 μg, all of which is attributable to platinum evaporation. Capsules were weighed before and after all runs. Any experiments with detectable weight loss were discarded. The weight measurements were made with a Mettler Toledo UMX2 ultra-microbalance with a precision of 0.2 μg.

Determination of H_2O content of charges

The H_2O content of charges was determined with use of a precision microbalance using techniques developed in this laboratory to quantitatively seal H_2O into platinum capsules. Given negligible sealing loss relative to H_2O input into the capsule and retrieval of capsules without detectable weight loss after the experiment, we unambiguously determine the bulk H_2O content of run products without recourse to indirect techniques such as Raman, FTIR, Karl Fischer titration, EMPA, ion probe, gravimetric analysis, etc., all of which can be prone to significant analytical uncertainty. Bartoli et al. (2016) give a summary of analytical uncertainties using these techniques, which can be as great as 20% relative to the amount of H_2O actually contained in quenched glass.

Two additional points may be made to emphasize the validity of this method for H_2O determination of charges. First, Truckenbrodt and Johannes (1999) investigated H_2O loss from piston–cylinder experiments using platinum capsules and found that no detectible loss for samples run at $T \leq 1050$ °C, 1.0 GPa, for run times up to 6 days. Second, Newton and Manning (2008) and Tropper and Manning (2007) found no capsule weight losses in experiments, where crystal solubilities were measured at temperatures up to 1100 °C at 1.0 GPa. Newton and Manning (2006; 2007) showed H_2O-in measurements to be nearly identical to H_2O-out measurements by puncturing capsules after the run and measuring H_2O by drying loss.

Piston–cylinder methods

All experiments were carried out in a piston–cylinder apparatus of 2.54 or 1.91 cm diameter with graphite heater sleeves and NaCl pressure medium. For runs at $T > 900$ °C, pressed boron nitride (BN) spacers 0.35 cm thick were placed above and below the capsule to prevent melting of the pressure medium. Pressure calibrations based on the solubility of quartz in H_2O (Newton and Manning 2008) necessitate a -0.06 GPa pressure correction, which was applied to all relevant reported experimental pressures. No pressure

correction was necessary for the all-NaCl furnace assembly. Pressures were monitored on a Heise bourdon tube gauge and are believed accurate to ± 0.03 GPa (Johannes et al. 1971). Temperatures were controlled and monitored digitally using an S-type thermocouple (uncertainty ± 3 °C; no correction for the effect of pressure on emf). The 2–3-mm-thick capsules were loaded transversely to the heater cylinder to minimize the temperature gradient across the sample. An assembly was cold pressed to 0.75 GPa and then heated. As pressure rose upon heating, the pressure was bled to maintain a nominal pressure of 1.0 GPa. For multi-step experiments, where the temperature was lowered, the pressure was increased during the run to maintain the desired 1.0 GPa. Runs were terminated by quenching to <200 °C in <30 s by turning off the heating power.

Analytical methods

In many experiments, the quenched charge could be removed largely intact from the platinum capsule by making an incision, then removing the glassy slug with tweezers. Opposite sides of this slug were ground and polished to make a thick section for optical microscopy. Portions of many charges were disaggregated in a mortar and pestle, and the fragments were further investigated with and without immersion oils. Samples selected for scanning electron microscope (SEM) petrography were mounted in epoxy resin, polished with water based diamond paste, and studied with a Tescan Vega-3 XMU scanning electron microscope using backscattered electron (BSE) and cathodoluminescence (CL) imaging.

Representative charges studied by SEM petrography were used for determination of phase compositions by electron microprobe analyzer (EMPA). We used a JEOL 8500 instrument in the Department of Earth, Planetary and Space Sciences at UCLA. Operating conditions for the analysis of crystals were 15 kV, 15 nA, and a 2-μm beam spot size. Counting times were 20 s on the sample and 5 s on background for all elements except the alkali metals (10 s sample and 5 s background). For analysis of hydrous glasses, the beam was defocused to 14 μm and the current lowered to 6 nA to minimize H and Na loss (Morgan and London 1996; 2005). Counting times were 20 s on the sample and 5 s on background. The standards used were a Tiburon, California, albite (Si, Al, and Na), a St. Gottard, Switzerland, adularia (K) and a Great Sitkin Island, Alaska, anorthite (Ca). Particular attention was paid to characterization of subtle textures of crystallization (and sometimes resorption) that were identified by optical and SEM study.

Portions of nearly all samples were ground and analyzed using the PANalytical Powder X-ray diffractometer (XRD) in the UCLA Chemistry Department with Cu Kα ($\lambda = 1.5408$ Å) radiation. Scans were collected in the range

of $20° \leq 2\theta \leq 28$, 34 or $60°$ at a rate of either $2°$ per 60 s for routine phase identification or at a much slower rate of $0.017° \ 2\theta$ steps per 60 s for a single sample on which a unit cell refinement of the feldspar was performed. The (111) peak from a high purity silicon wafer at $28.440° \ 2\theta$ was used to calibrate and index the diffraction peaks when the goal was only phase identification, whereas an annealed fluorite (CaF_2) internal standard (McMurdie et al. 1985) was used to calibrate and index the diffraction peaks for the feldspar unit cell refinement. For the unit cell refinement, peak positions were converted to unit cell lengths and volumes of crystalline products using the UnitCell OSX program of Holland and Redfern (1997). For samples that contained less than approximately three volume percent crystals, phase identification by petrographic microscopy was more accurate because of detection limitations due to vanishingly small diffraction peaks above the high background characteristic of glassy samples.

Results

Compositions, conditions, and results of experiments are summarized in Table 1. The bulk H_2O contents of individual experiments were typically within 3% of the target value. Demonstration of the equilibrium liquidus T required a complex run procedure because of severe problems of supercooling, metastable crystallization, and sluggish formation and resorption of crystals. At fixed pressure and a given H_2O content, we found that three temperature stages were needed, requiring as many as eight multi-step experiments to bracket the liquidus to within ±25 °C at each investigated bulk composition. Below, we first provide an overview of the reversal strategy before describing textures, compositions, and our new constraints on the liquidus as a function of temperature at 1.0 GPa.

Reversal strategy

Melt homogenization

The nominally simple strategy of locating the liquidus minimum by raising temperature on crystalline mixtures with H_2O until evidence for 100% liquid is seen leads to serious inaccuracy that results from slow melting and generation of strongly heterogeneous liquid compositions. Therefore, it was necessary to remelt the starting glass, with the desired amount of H_2O, at temperature and time sufficient to homogenize to a single-phase liquid prior to lowering the temperature at constant pressure in a search for the first crystallization products (e.g., Webster 1997). Charges were held at a temperature (homogenization temperature, T_H) well above that of the liquidus for time (homogenization time, t_H)

(Table 1), as predicted from previous work. This ensured that the added water and any SiO_2-rich zones remaining from 1-atm fusion were digested and homogeneously distributed in the melt.

A subset of experiments for certain compositions at low H_2O (runs G1, 2, and 5; Table 1) were quenched from the homogenization temperature to check that nominal superliquidus temperature was exceeded and homogeneity achieved. All returned homogeneous crystal-free glass. For subsequent runs, homogenization temperatures were 1050 °C for charges with 3 wt% H_2O, ≥950 °C for 4.1 wt% H_2O, and ≥850 °C for charges with 5.8, 8.0, and 12.0 wt% H_2O. The time for melt homogenization in all experiments was >4 h (Table 1).

Step 1: initial crystallization

After holding a charge at superliquidus conditions, T was lowered in a search for conditions at which feldspar and quartz crystallized directly from a homogeneous hydrous melt. The charges were typically held at the lower T for ~72 h (Table 1). We found that in most cases, 2 days were insufficient to nucleate and grow crystals in undercooled melts. Other workers have also noted problems of crystallization from granitic liquids that were undercooled (e.g., London et al. 1989; Nabelek et al. 2010). Moreover, many of the crystals optically identified as feldspar gave microprobe analyses with excess silica and were interpreted to be metastable. Therefore, single-step experiments only identified a minimum value for the liquidus T at a particular composition.

Step 2: reversal of liquidus

To establish an equilibrium liquidus T, the temperature of an initially homogenous charge of a given H_2O content was crystallized at a lower temperature T_1 for time t_1 (step 1 in Table 1) and then raised to temperature T_2 for time t_2 (step 2 in Table 1). In a typical two-step experiment, the apparently silica-rich nonstoichiometric feldspars that formed at a lower temperature were partially resorbed, and a new generation of stoichiometric feldspars grew. The highest temperature at which the new generation of feldspar and quartz formed represents the lower bound of the liquidus for a specific bulk composition and pressure. At a slightly higher temperature, the last remnants of crystals were resorbed into the liquid. This temperature represents the upper bound on the liquidus for that same bulk composition and pressure.

Textures of run products

Homogenized liquids quenched to optically isotropic, apparently homogeneous glass. Glasses from runs at 3.0 and 4.1

Table 1 Experimental results at 1.0 GPa

Run	Qz (wt%)	H_2O (wt%)	T_H (°C)	T_1 (°C)	T_2 (°C)	t_H (h)	t_1 (h)	t_2 (h)	Result
G50	25	2.939	1050	950		17	75		L
G40	25	3.021	1050	900		20	70		L + fsp + qz
G41	25	3.016	1050	850		17	144		L + fsp + qz
G45	25	3.032	1050	800		17	51		L + fsp + qz
G99	25	2.849	1050	900	1000	6	70	102	L
G91	25	3.046	1050	900	1000	21	70	103	L
G87	25	2.914	1050	900	950	16	74	74	L + fsp + qz
G46	25	3.063	1050	800	875	19	72	54	L + fsp + qz
G58	27.5	3.054	1050	935		18	48		L
G55	27.5	3.052	1050	900		19	98		L + fsp + qz
G65	27.5	3.054	1000	900		4	89		L + fsp + qz
G79	27.5	3.033	1050	900	985	17	75	72	L
G72	27.5	3.015	1050	900	935	18	72	150	L + fsp + qz
G56	30	3.040	1050	1000		20	48		L
G52	30	3.039	1050	950		23	24		L + qz
G36	30	3.039	1050	900		19	48		L + qz
G39	30	2.972	1050	850		21	71		L + fsp + qz
G104	30	3.031	1050	850	1000	14	72	101	L
G89	30	3.026	1050	850	950	16	88	104	L + fsp + qz
G49	30	2.994	1050	850	900	18	75	52	L + fsp + qz
G44	30	3.018	1050	850	900	20	73	89	L + fsp + qz
G5	20	4.129	950			69			L
G8	20	4.153	950	850		23	120		L + fsp
G48	20	4.124	1000	800		15	48		L + fsp + qz
G10	25	4.164	950	900		69	47		L
G12	25	4.229	950	800		66	99		L + fsp + qz
G96	25	4.057	1050	800	950	21	47	72	L
G97	25	4.152	1050	800	900	17	72	103	L
G15	25	4.092	950	800	850	93	96	342	L + fsp + qz
G14	25	4.164	950	800	850	69	96	72	L + fsp + qz
G74	27.5	4.120	1050	900		25	93		L
G62	27.5	4.102	1050	875		17	77		L
G69	27.5	4.075	900	850		67	74		L + fsp + qz
G54	27.5	4.114	1050	850		20	98		L + fsp + qz
G63	27.5	4.115	1050	825		14	221		L + fsp + qz
G82	27.5	4.096	1050	800	915	46	71	27	L
G100	27.5	3.840	1050	800	900	20	73	93	L
G93	27.5	4.178	1050	800	875	20	71	148	L + fsp + qz
G1	30	4.054	950			52			L
G3	30	4.167	950	900		71	70		L + fsp + qz
G11	30	4.116	950	800		66	99		L + fsp + qz
G83	30	3.768	1050	900	950	24	80	86	L
G108	30	4.128	1050	800	900	19	73	71	L + fsp + qz
G35	30	4.103	950	800	850	43	74	165	L + fsp + qz
G13	30	4.147	950	800	850	69	96	72	L + fsp + qz
G30	25	5.850	900	800		48	77		L
G34	25	5.859	900	775		44	119		L + fsp + qz
G29	25	5.884	900	750		67	95		L + fsp + qz
G47	25	5.846	900	700		19	52		L + fsp + qz
G80	25	5.891	900	775	850	68	70	126	L
G28	25	5.797	900	750	800	45	74	95	L + fsp + qz

Table 1 (continued)

Run	Qz (wt%)	H_2O (wt%)	T_H (°C)	T_1 (°C)	T_2 (°C)	t_H (h)	t_1 (h)	t_2 (h)	Result
G51	25	5.862	900	700	750	14	75	52	L + fsp + qz
G75	27.5	5.853	900	825		92	98		L
G68	27.5	5.857	900	775		24	47		L + fsp + qz
G66	27.5	5.864	900	775		71	27		L + fsp + qz
G73	27.5	5.873	900	750		69	100		L + fsp + qz
G76	27.5	5.817	900	775	825	72	75	99	L
G101	27.5	5.867	900	750	800	25	84	92	L
G2	30	5.841	850			65			L
G26	30	5.819	900	800		46	71		L + qz
G33	30	5.822	900	775		44	119		L + fsp + qz
G25	30	5.822	900	750		41	71		L + fsp + qz
G81	30	5.894	900	800	850	66	70	120	L
G27	30	5.823	900	750	800	45	74	95	L + fsp + qz
G20	25	8.102	850	750		44	70		L
G19	25	8.147	850	750		90	74		L
G23	25	8.101	850	700		25	70		L + fsp + qz
G17	25	8.277	850	700		94	96		L + fsp + qz
G57	25	7.961	900	675		70	192		L + fsp + qz
G53	25	7.946	900	650		23	103		L + fsp + qz
G92	25	7.919	900	700	800	68	69	98	L
G88	25	8.038	900	700	750	67	69	113	L + fsp
G60	27.5	8.065	900	725		98	93		L
G64	27.5	7.902	900	700		18	70		L + fsp + qz
G95	27.5	7.928	900	700	775	73	89	168	L
G77	27.5	7.971	900	700	750	69	75	96	L + fsp
G67	27.5	7.878	900	700	725	21	69	65	L + fsp + qz
G21	30	7.874	850	750		44	70		L
G61	30	8.006	900	725		98	93		L + fsp + qz
G22	30	7.902	850	700		25	70		L + fsp + qz
G16	30	7.832	850	700		94	96		L + fsp + qz
G90	30	7.962	900	725	800	74	70	120	L
G84	30	7.888	900	725	775	45	60	77	L + qz
G24	30	7.904	850	700	750	45	48	121	L + fsp + qz
G31	25	11.992	900	675		50	123		L + qp
G43	25	11.481	900	650		69	98		L
G38	25	12.048	900	625		40	123		L + fsp + qz (+qp)
G103	27.5	11.970	900	625		22	95		L + fsp + qz (+qp)
G107	27.5	12.069	900	625	700	4.5	84	102	L
G102	27.5	11.979	900	625	675	25	84	108	L (+qp)
G94	27.5	12.003	900	625	650	20	74	167	L + fsp + qz (+qp)
G32	30	12.130	900	675		50	123		L
G42	30	11.990	900	650		69	98		L + qz
G37	30	12.004	900	625		40	123		L + fsp? + qz (+qp)

Qz indicates anhydrous concentration of SiO_2 in excess of that present in an equal weight mixture of Ab and Or, normalized to 100 wt% (e.g., if Qz = 30, then Ab = Or = 35 wt% in the starting anhydrous composition). T_H and t_H refer to the melt homogenization temperature and time, respectively. T_1 and T_2 indicate temperatures of successive steps in an experiment (see text). t_1 and t_2 indicate time in hours at which the experiment was held at each T

L liquid, *fsp* feldspar, *qz* quartz, *qp* quench product mica and/or devitrified gel, and *?* evidence inconclusive to positively identify phase

wt% H_2O were free of bubbles. Glasses quenched from experiments at higher H_2O content ranged from occasionally vesiculated (5.8 and 8.0 wt%) to always vesiculated (12.0 wt%).

The crystalline SiO_2 phase was typically skeletal dagger-shaped of β-quartz morphology in runs at >750 °C, and had equant α-quartz morphology at lower T, in agreement with the stability fields of these polymorphs (Cohen and Klement 1967). Crystals were typically <40 μm long in any direction and dispersed throughout the charge (Fig. 2).

Crystals with the optical properties of feldspar formed clusters that typically had a subspherical rosette texture (Fig. 2a, b) similar to those described by Arzilli and Carroll (2013) and Arzilli et al. (2015). CL imaging reveals that the clusters are comprised of numerous individual prismatic crystals, as in the core of the feldspar rosette

Fig. 2 BSE photomicrographs of run product textures in two-step experiments. **a** Overview of a glassly slug removed from a typical two-step crystallization experiment which exhibits rosettes of feldspar-1 (fsp-1) crystals set in matrix of glass and β-quartz (Run G11; Table 1). **b** Magnification of **a** showing feldspar-1 rosettes and quartz (qz) in glass matrix (Run G11). Star-shaped β-quartz skeletal crystals are uniformly distributed in glass matrix and included in euhedral feldspar-1, suggesting that quartz was the first-nucleating phase as verified by experiments, as shown in Table 4 (see below). **c** Magnification of a rim from a feldspar-1 rosette in Fig. 2a (Run G11) showing intergrowth of quartz and feldspar-2 (fsp-2). **d** Large feldspar-morphology crystal outline showing discrete sectors comprised of graphic granite-like intergrowths of anhedral quartz and feldspar-2 (Run G63; Table 2, see below). **e** Portion of feldspar-morphology crystal termination showing complex intergrowth of feldspar-2 and quartz. The size of quartz grains decreases toward the interior (Run G73). **f** Skeletal "hopper" feldspar-2 crystals cored by glass (*dark*) and feldspar–quartz intergrowths (Run G48; Table 3)
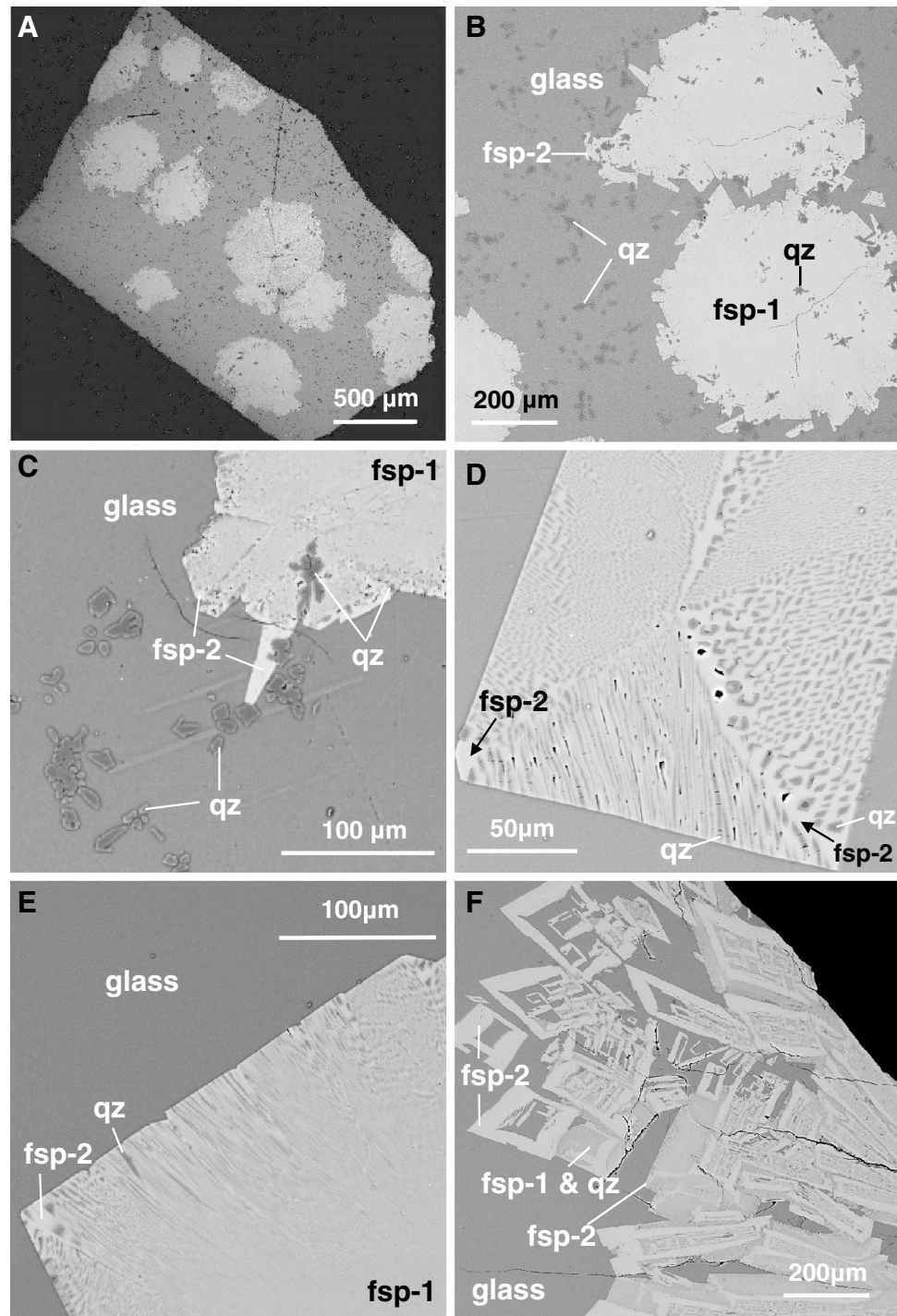
Fig. 3 SEM photomicrographs of run products from three-step reversal experiments. **a** BSE image of partially resorbed feldspar-1 (fsp-1) rosette in glass matrix. Original extent of rosette is outlined by new generation of small, stoichiometric feldspar-2 (fsp-2), and quartz (Run G51; Table 1). **b** CL image of partially resorbed feldspar-1, rimmed by skeletal feldspar-2 and quartz. CL imaging reveals that feldspar-1 rosettes are aggregates of numerous individual crystals (Run G14; Table 1). **c** BSE image of skeletal feldspar-2 and quartz (Run G28; Table 1). The outline and texture suggest that larger, early-formed feldspar-1 has been almost entirely resorbed
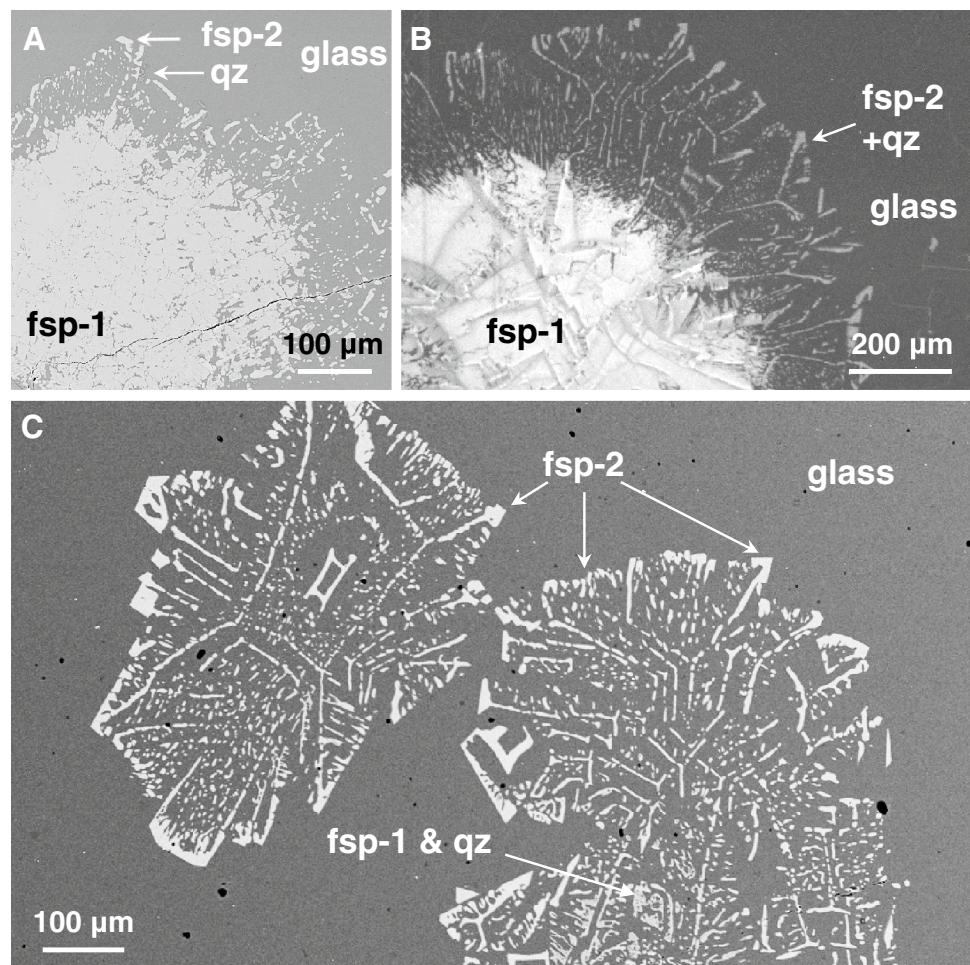
in Fig. 3b. The feldspar phase in the cores of the clusters coexists with euhedral-to-subhedral quartz and appears compositionally homogeneous when observed with BSE (Fig. 2b). However, in some cases, the rims of the clusters are complex feldspars with euhedral terminations intergrown with anhedral quartz (Fig. 2c–e). The feldspar phase commonly has slightly higher BSE intensity than in the cores. The quartz in the intergrowths ranges from elongate, lamellar crystals to equant, anhedral crystals that form myrmekitic to granophyric textures. The intergrowths are often seen in sector-zoned grains which display graphic texture (Fig. 2d), similar to that reported by Fenn (1977, 1986). It is a general feature that rosettes formed during one-step runs exhibit a high degree of homogeneity in the core as examined by optical or SEM techniques, whereas the rims of those same rosettes exhibit quartz intergrowths (Fig. 2b, c). The extent of the development of intergrowths in the clusters may correlate with time: in Run G11 (Fig. 2b, c; 99 h), the clusters show quartz intergrowths in the outer tens of microns, and in Run G63 (Fig. 2d; 221 h), most of the cluster mass has converted to graphic-textured intergrowths. However, time is likely not

the only pertinent factor; we did not control for Qz or H_2O content, or degree of potential undercooling. For example, Run G48 with Qz_{20} (Fig. 2f; 48 h) yielded composite hopper crystals with fine quartz intergrowths.

To distinguish between the two feldspar types, we refer to the apparently homogenous feldspar phase found in rosette cores as feldspar-1 and the texturally distinct feldspars either forming at rims in complex intergrowth with quartz or in two-step experiments (see below) as feldspar-2 (Figs. 2, 3). As shown in Sect. 3.3, feldspar-1 is a stoichiometric feldspar of variable K/Na intergrown with optically unresolvable quartz, whereas feldspar-2 is stoichiometric feldspars of a limited K/Na value.

We conducted an additional set of experiments to establish the order of crystallization of feldspar-1 and quartz. The experiments were at 4.0 ± 0.1 wt% H_2O and $Qz_{27.5}$ (Table 2). All samples were melted at 1050 °C for ≥13 h. The temperature was then lowered to 800 °C for 6–72 h. At 800 °C, crystals with β-quartz morphology nucleated and grew within 6–24 h. Feldspar-1 rosettes began to form between 24 and 35 h, and their size increased when run times were longer. Thus, quartz nucleation and growth precedes feldspar-1,

Table 2 Results of experiments on order of crystallization at 1.0 GPa

Run	Qz (wt%)	H_2O (wt%)	T_1 (°C)	T_2 (°C)	t_1 (h)	t_2 (h)	Result
GK-1	27.5	4.118	1050	800	23	6	L
GK-2	27.5	4.108	1050	800	16	24	L + qz
GK-5	27.5	3.911	1050	800	13	35	L + fsp + qz
GK-4	27.5	4.065	1050	800	21	48	L + fsp + qz
GK-3	27.5	4.056	1050	800	21	72	L + fsp + qz

Explanation: see Table 1

consistent with the observed inclusions of euhedral quartz in some rosettes (Fig. 2b).

Quartz from two-step experiments is fine-grained, but tends to be more equant than in one-step experiments (Fig. 3a). Feldspars show a range of textures. In some runs, rosettes or clusters of feldspar-1 similar to those observed in two-step subliquidus runs are present, but their rims appear to have reacted with the liquid to produce fine-grained (<30 μm), generally subhedral-to-anhedral feldspar-2 grains coexisting with quartz and surrounded by liquid (Fig. 3a, b). In some cases, no feldspar-1 rosettes are preserved, but outlines of their original shapes are defined by intricate skeletal feldspar-2 and quartz structures (Fig. 3c). The textures are consistent with formation during incomplete resorption of feldspar-1 rosettes and clusters that grew during the second experimental step, with production of feldspar-2 and quartz. Thus, the textures suggest that the final subliquidus equilibrium feldspar is feldspar-2.

Phase compositions and properties

The compositions of glasses, feldspar-1, and feldspar-2 were determined by EMPA (Tables 3, 4). Quartz was verified with EMPA.

Selected glass compositions were determined in experiments in one-step and two-step runs in which no crystals were observed and vapor bubbles were largely absent (i.e., bulk H_2O less than ~8 wt%; Table 2). Glasses in runs with 12 wt% H_2O were not analyzed, because the required beam diameter was larger than the spacing of vesiculation bubbles. The crystal-free glass analyses provide a check on compositional fidelity of the experiments. Average quenched crystal-free glass compositions are reported in Table 3. We numerically estimated the error in analyzed glass compositions using a simple Monte Carlo routine (1000 simulations) and the standard deviation in the means of the analyses. Each nominal bulk composition is within 2σ of the mean analyzed composition. In addition, the analyzed glasses consistently show minor amounts of normative corundum or Na silicate (Table 3). We attribute the small compositional disparities to the challenges of analyzing Na in hydrous granitic glasses.

Representative compositions of glasses coexisting with feldspar-1 and quartz in one-step experiments are shown in Fig. 4a–c. The glasses have normative Qz similar to their respective bulk compositions, but Or contents are lower. Estimated errors are notably larger than those of crystal-free glasses, suggesting that crystallization in one-step experiments has induced compositional changes in the liquid which are preserved in the quenched glasses.

Analyses of feldspar from one-step runs revealed substantial compositional complexity, consistent with the textural complexity described above. Analysis of feldspar-1 showed apparent nonstoichiometry (Table 4). They typically have excess Si with resulting compositions plotting with a Qz component in the Ab–Or–Qz ternary (Fig. 4). Al contents are correspondingly low, and the crystals have low total cations on an eight-oxygen basis. In contrast, where they are present in one-step runs, feldspar-2 crystals are stoichiometric alkali feldspar (Table 4).

We performed X-ray powder diffraction on the persiliceous feldspar-1 rosette from Run G45 (Table 1). The rosette in this sample has varying degrees of homogeneity, with the rims being more evolved than the cores, very similar to the sample, as shown in Fig. 2e. The diffraction pattern contains both quartz and feldspar peaks. The peaks used for the unit cell determination of feldspar-1 are given in Supplementary Table 1. The peaks were identified according to the indexing of sanidine used by Wright and Stewart (1968). The monoclinic unit cell parameters, calculated using UnitCell (Holland and Redfern 1997), are $a = 8.397 \pm 0.003$Å, $b = 12.991 \pm 0.002$Å, $c = 7.160 \pm 0.002$Å, $\beta = 116.07 \pm 0.02$, unit cell volume = 701.625 ± 0.248 Å^3 (95% confidence level). Values for the unit cell constants in G45 feldspar-1 are all nearly identical to those given by Orville (1967) for synthetic sanidine at the same molar K/Na (Supplementary Fig. 1).

Representative compositions for two-step experiments are shown in Fig. 4d–f. As in one-step runs, the glasses have normative Qz similar to their respective bulk compositions. Or contents are generally lower; where crystal contents are low (e.g., Run G24, Fig. 4f), the glass and bulk compositions are nearly identical. Estimated errors are lower than in one-step experiments (Fig. 4), suggesting that the additional step leads to more homogeneous liquid compositions.

The apparent composition of incompletely resorbed feldspar-1 remains nonstoichiometric (Table 4; Fig. 4d, e).

Table 3 Average compositions of run product glasses

	G56	G56 nominal	G74	G74 nominal	G75	G75 nominal	G45
n	9		15		10		10
SiO_2	73.82	74.39	72.27	71.97	70.22	70.67	70.67
Al_2O_3	12.89	12.81	13.18	13.58	12.71	13.33	13.60
Na_2O	4.16	4.01	4.22	4.25	4.02	4.17	4.54
K_2O	5.67	5.74	5.76	6.08	5.64	5.97	5.33
Total	96.55	96.95	95.42	95.88	92.59	94.14	94.15
CIPW norm							
Ab	35.99	35.00	37.41	36.25	36.70	36.25	40.84
Or	34.71	35.00	35.66	36.25	35.99	36.25	33.48
Qz	29.19	30.00	26.93	27.50	27.31	27.50	25.30
Co	0.00		0.00		0.00		0.38
NS	0.11		0.00		0.01		0.00
	G46	G63	G48	G28	G51	G73	G24
n	10	10	10	10	10	9	10
SiO_2	71.39	70.84	67.88	68.78	67.92	69.01	68.48
Al_2O_3	13.76	12.98	14.40	13.47	12.91	12.53	12.36
Na_2O	4.59	4.51	4.95	4.40	4.48	4.31	3.64
K_2O	5.37	5.04	4.98	5.37	4.58	4.81	5.25
Total	95.12	93.38	92.20	92.02	89.89	90.65	89.73
CIPW norm							
Ab	40.80	40.90	45.39	40.48	42.19	40.22	34.29
Or	33.38	31.89	31.90	34.50	30.10	31.34	34.60
Qz	25.40	27.10	21.76	24.58	27.06	28.19	30.34
Co	0.42	0.11	0.95	0.44	0.65	0.26	0.77
NS	0.00	0.00	0.00	0.00	0.00	0.00	0.00

All compositions in wt% determined by electron microprobe analysis; see text for analytical conditions. Starting bulk compositions indicated by Qz and H_2O contents (wt%). Compositions are averages of n individual analyses. Abbreviations, as shown in Table 1, except: *Co* corundum, *NS* Na silicate. Nominal compositions of starting glasses presented for comparison in runs containing no crystals

Feldspar-2 in two-step runs is stoichiometric alkali feldspars that are substantially more potassic than the coexisting melt phase, as is typical for hypersolvus sanidines (Parsons 1978). We found no evidence for crystallization of two coexisting feldspars.

The reversed liquidus minimum at 1.0 GPa

The upper temperature limit for coexisting feldspar and quartz in two-step runs defines the liquidus minimum at any H_2O content. We evaluated the role of Qz by determining the liquidus at concentrations of 25, 27.5, and 30 wt% Qz and 3.0, 4.1, 5.8, 8.0, and 12.0 wt% H_2O (Fig. 5). If Or/Ab = 1 yields the ternary liquidus minimum at a given Qz and H_2O content (Fig. 1), then a two-step experiment constrains this minimum to lie between the highest temperature at which both feldspar-2 and quartz stably coexist with liquid and the lowest temperature at which no crystals were detected. Strictly speaking, this result at our fixed Or/Ab to bulk ratio of 1 does not uniquely define the liquidus minimum at 8.0

and 12.0 wt% H_2O (see Fig. 1), but should be a good approximation to the true minimum for lower H_2O contents.

At 3.0 wt% H_2O, runs at Qz_{25}, $Qz_{27.5}$, and Qz_{30} yield brackets of 950–1000, 935–985, and 950–1000 °C, respectively (Fig. 5a). The appearance of a lower T bracket at $Qz_{27.5}$ may suggest that this composition is close to an absolute temperature minimum. The results, however, do not support the inference of a variation greater than 25 °C in the T brackets with varying Qz content.

At 4.1 wt% H_2O, runs at Qz_{25}, $Qz_{27.5}$, and Qz_{30} yield brackets of 850–900, 875–900, and 900–950 °C, respectively (Fig. 5b). The results could be interpreted as reflecting increasing liquidus temperature with Qz; however, this could simply be a consequence of the different bracket widths at Qz_{25} and $Qz_{27.5}$ (50 vs. 25 °C; Fig. 5b).

At 5.8 wt% H_2O, runs at Qz_{25} and Qz_{30} yield brackets of 800–850 °C (Fig. 5c). Both two-step runs at $Qz_{27.5}$ (at 800 and 825 °C) yielded liquid only. When combined with subliquidus one-step runs G66 and G68 at 775 °C (Table 1), a bracket of 775–800 °C can be inferred, which could be

Table 4 Average compositions of feldspars

	G45 Feldspar-1	G46 Feldspar-1	G46 Feldspar-2	G48 Feldspar-2	G63 Feldspar-2	G28 Felsdpar-2
Qz	25	25	25	20	27.5	25
H_2O	3.0	3.1	3.1	4.1	4.1	5.8
n	9	9	10	11	6	8
SiO_2	74.33	74.51	66.69	66.90	66.36	65.50
Al_2O_3	14.81	14.98	19.47	19.52	19.25	19.13
Na_2O	4.01	4.30	5.50	4.57	4.82	3.46
K_2O	7.20	6.98	9.17	10.58	10.09	12.22
Total	100.36	100.78	100.84	101.57	100.53	100.31
Si	3.243	3.237	2.981	2.982	2.985	2.978
Al	0.762	0.767	1.026	1.025	1.020	1.025
Na	0.340	0.363	0.477	0.395	0.421	0.305
K	0.401	0.387	0.523	0.602	0.579	0.709
Total	4.746	4.754	5.006	5.004	5.005	5.017
	G51 Feldspar-1	G51 Feldspar-2	G73 Felsdpar-1	G73 Felsdpar-2	G24 Feldspar-2	
Qz	25	25	27.5	27.5	30	
H_2O	5.9	5.9	5.9	5.9	7.9	
n	7	9	3	4	7	
SiO_2	73.99	66.40	72.23	66.24	65.56	
Al_2O_3	14.64	19.11	15.52	19.03	18.65	
Na_2O	2.25	4.27	2.49	3.50	2.31	
K_2O	9.80	10.85	10.40	12.07	13.68	
Total	100.68	100.62	100.64	100.83	100.2	
Si	3.247	2.990	3.193	2.990	2.996	
Al	0.757	1.014	0.809	1.012	1.005	
Na	0.192	0.373	0.213	0.306	0.205	
K	0.549	0.623	0.586	0.695	0.797	
Total	4.745	5.000	4.802	5.004	5.003	

All compositions in wt% and determined by electron microprobe analysis; see text for analytical conditions. Starting bulk compositions indicated by Qz and H_2O contents (wt%). Compositions are averages of *n* individual analyses. Abbreviations, as shown in Table 1, except: *Co* corundum, *NS* Na silicate. Nominal compositions of starting glasses presented for comparison in runs containing no crystals

evidence for a slight minimum in the liquidus temperature near Qz$_{27.5}$.

At 8.0 wt% H_2O, runs at Qz$_{27.5}$ and Qz$_{30}$ yield brackets of 725–775 and 750–800 °C (Fig. 5d). Applying the same logic as at 5.8% H_2O, Qz$_{25}$, the results at 8% H_2O and Qz$_{25}$ yield a broad bracket of 700–800 °C. Runs at 750 °C, Qz$_{25}$ and Qz$_{27.5}$ both contained secondary feldspar but no quartz, whereas the run at 775 °C, Qz$_{30}$ contained quartz but no feldspar. Therefore, the liquidus minimum must lie between Qz$_{27.5}$ and Qz$_{30,}$ and 725 and 775 °C.

Taking the results at the four H_2O contents together, we find no certain dependence of liquidus minimum temperature on Qz component at the level of resolution of this study (Fig. 5). At all conditions studied, the two-phase loops (liquid + feldspar and liquid + quartz) must span a very narrow T range at 25–30% Qz, consistent with proximity to the true minimum (or eutectic at high H_2O; Fig. 1). The liquidus temperature minima reported at 3.0, 4.1, 5.8, 8.0,

and 12.0 wt% are, respectively, 935–985, 875–900, 775–800, 725–775, and 650–675 °C (Fig. 6). The temperature intervals most nearly bracket the ternary liquidus minima for the lower H_2O contents; though for the highest two H_2O contents investigated, our reported bracket for Or/Ab = 1 may be slightly high in temperature (Fig. 1). Figure 6 shows two-step experimental brackets that most tightly constrain the liquidus minimum temperature for all Qz and bulk H_2O compositions investigated. We combined bracket midpoints from Fig. 6 at 27.5 wt% Qz and Or/Ab = 1 with the solidus temperature of 635 °C at 17.0 wt% H_2O (Luth et al. 1964) and the extrapolated 0.8 GPa result of Holtz et al. (2001a) at 1 wt% H_2O (1090 °C) to obtain the following equation for the reversed haplogranite liquidus curve at 1.0 GPa:

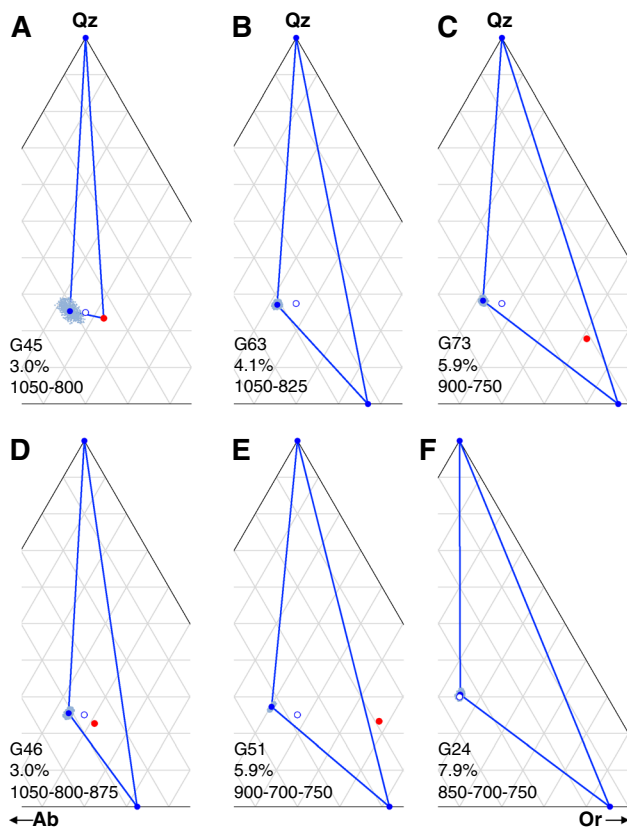$$T = -0.0995 w_{H_2O}^3 + 5.0242 w_{H_2O}^2 - 88.183 w_{H_2O} + 1171.0$$
$$(1)$$

Fig. 4 Partial Ab–Or–Qz ternary diagrams showing compositions of selected experiments. Lower left in each ternary gives experiment number, bulk H_2O (wt%), and temperature at each experimental step. *Open circles* dry bulk composition; *filled blue circles* quartz, feldspar-2, or normative glass composition; *filled red circles* feldspar-1; *small light blue dots* glass compositions from Monte Carlo simulations that are $\leq 2\sigma$ in the mean of each normative component (based on 1000 simulations). **a–c** Compositions from selected one-step experiments containing glass and crystals. **d–f** compositions from selected two-step reversal experiments containing glass and crystals

where w_{H_2O} is in wt% and T is in °C. A graphically extrapolated dry melting temperature of 1167 °C (Holtz et al. 2001a) was used to guide the fit. The extrapolated dry melting temperature for haplogranite obtained from Holland and Powell (2001) agrees closely with our reported value.

Discussion

Attainment of equilibrium and nonstoichiometric feldspar

Our experiments show that determination of liquidus $T - X_{H_2O}$ relations using initially homogeneous liquid starting material and the traditional one-step approach is insufficient because of undercooling and metastable crystallization. This strategy yielded charges in which quartz

crystallized first, followed by apparently nonstoichiometric, persiliceous feldspar-1 rosettes. Unit cell refinement of feldspar-1 indicated, however, that the excess silica is not in solid solution as Si_4O_8 in the feldspar structure, but exists as submicroscopic quartz intergrowths. The crystallization of feldspar-1 introduced compositional heterogeneity in the liquid (Fig. 4). Experiments held at step-1 temperatures for longer times tended to show textures indicating reaction of feldspar-1 to produce stoichiometric feldspar-2 and quartz on rosette margins. This reaction never went to completion, even after >200 h. These experiments provide absolute lower temperature bounds on the feldspar–quartz cotectic at any H_2O content, since the liquids were demonstrably undercooled.

These textural and compositional data imply that, in the absence of nuclei in the starting material, there is a nucleation barrier in undercooled liquids at all H_2O contents investigated. Failure of nucleation of stable feldspar and nucleation and metastable growth of feldspar–quartz intergrowths in undercooled hydrous siliceous liquids have been reported in several experimental studies at lower pressures (Fenn 1977; Baker and Freda 2001; Waters and Andrews 2016).

Upper bounds on the cotectic temperature at a given H_2O content of the liquid were determined in the present study by two-step experiments, where a charge was held at the step 1 temperature long enough to ensure crystallization of quartz and feldspars, both feldspar-1 and feldspar-2, and then raised to a higher temperature for times longer than 3 days. At temperatures 25–50 °C above the step-1 temperature, the feldspar-1 was found to be variably resorbed, leaving only outlines of the former rosettes traced by stoichiometric feldspar-2 plus quartz (Fig. 3). Feldspar showed some degree of recrystallization and growth, and the surrounding liquid (glass) was more homogeneous than that surrounding the rosettes in the first stage product. It is inferred from this observation that the equilibrium (subliquidus) assemblage is feldspar-2 + quartz + liquid.

Experiments at the given H_2O content and still higher step-2 temperatures showed complete resorption of all crystalline phases, providing an upper bound on the liquidus minimum temperature. The liquidus minimum curve at 1.0 GPa consistent with the reversal experiments is shown in Fig. 6.

Comparison to previous work

Figure 6 compares our reversed brackets and liquidus minimum curve (Eq. 1) with liquidus minimum curves from Johannes and Holtz (1991) and Holtz et al. (2001a). The liquidus of Johannes and Holtz (1991) is based on graphical extrapolation of results from ≤0.5 GPa, so the comparatively poor agreement is unsurprising. Aranovich et al. (2014) reported a broad preliminary bracket of 800–900 °C at 1.0

Fig. 5 Summary of experimental results at 3.0, 4.1, 5.8, and 8.0 wt% ▶ H$_2$O as a function of Qz content. *L* liquid, *F* feldspar (undifferentiated feldspar-1 and feldspar-2 in one-step runs, feldspar-2 for two-step runs); *Q* quartz. *Squares* subliquidus one-step runs, *unfilled* for L + F+Q, *left filled* for L + F, *right filled* for L + Q. *Triangles* two-step runs, *filled* for L, *unfilled* for L + F+Q, *left filled* for L + F, *right filled* for L + Q. One-step runs offset by −3 °C where at same *T* and *Q* as a two-step run. *Gray rectangles* indicate the temperature *bracket* on the liquidus at each H$_2$O and Qz content shown

GPa and 4.1 wt% H$_2$O, but the experiments were unreversed one-step runs. The results of the present study indicate that the liquidus minimum for about 4% H$_2$O lies at the upper limit of this temperature range. Holtz et al. (2001a) obtained constraints at 0.8 GPa at 1 wt% H$_2$O. Differences of up to ~30 °C at >6 wt% H$_2$O may arise from our use of Or/Ab = 1, because the ternary minimum composition shifts from Or-rich to more Ab-rich as H$_2$O activity increases (Fig. 1). In light of this, the present experiments apply most rigorously to the equilibrium ternary liquidus minimum at low H$_2$O contents (high temperatures), and the liquidus temperatures for high H$_2$O contents may be somewhat closer to those advocated by Holtz et al. (2001a) than those based on our results. Nevertheless, at higher temperatures and lower H$_2$O contents, the present brackets correspond quite closely to those extrapolated from lower pressure data by Holtz et al. (2001a). It is important to note that, although the Qz content at the liquidus minimum may be expected to vary somewhat with the Or/Ab ratio, we detected little change in the liquidus temperature in the range 25–30 wt% Qz at any H$_2$O content (Fig. 5).

The new results combined with previous constraints portray the feldspar–quartz–liquid minimum or cotectic in the haplogranite–H$_2$O system as a function of temperature and pressure, as shown in Fig. 7. The H$_2$O isopleths extrapolated from lower pressures by Holtz et al. (2001a) have steeper dP/dT slopes (shown by dashed lines) at >6 wt% H$_2$O. The corresponding isopleths for H$_2$O-rich compositions in granite systems estimated by Clemens and Vielzeuf (1987) have even steeper dP/dT slopes than those of Holtz et al. (2001a).

Petrological interpretations

Feldspar solid solution and granophyric texture

Excess SiO$_2$ in synthetic and natural feldspars has been reported by several workers (Grundy and Ito 1974; Carman and Tuttle 1967; Perry 1968; Sturt 1970; Longhi and Hayes 1979). Megaw (1970) noted that sanidine and the coesite polymorph of SiO$_2$ are topologically equivalent, though
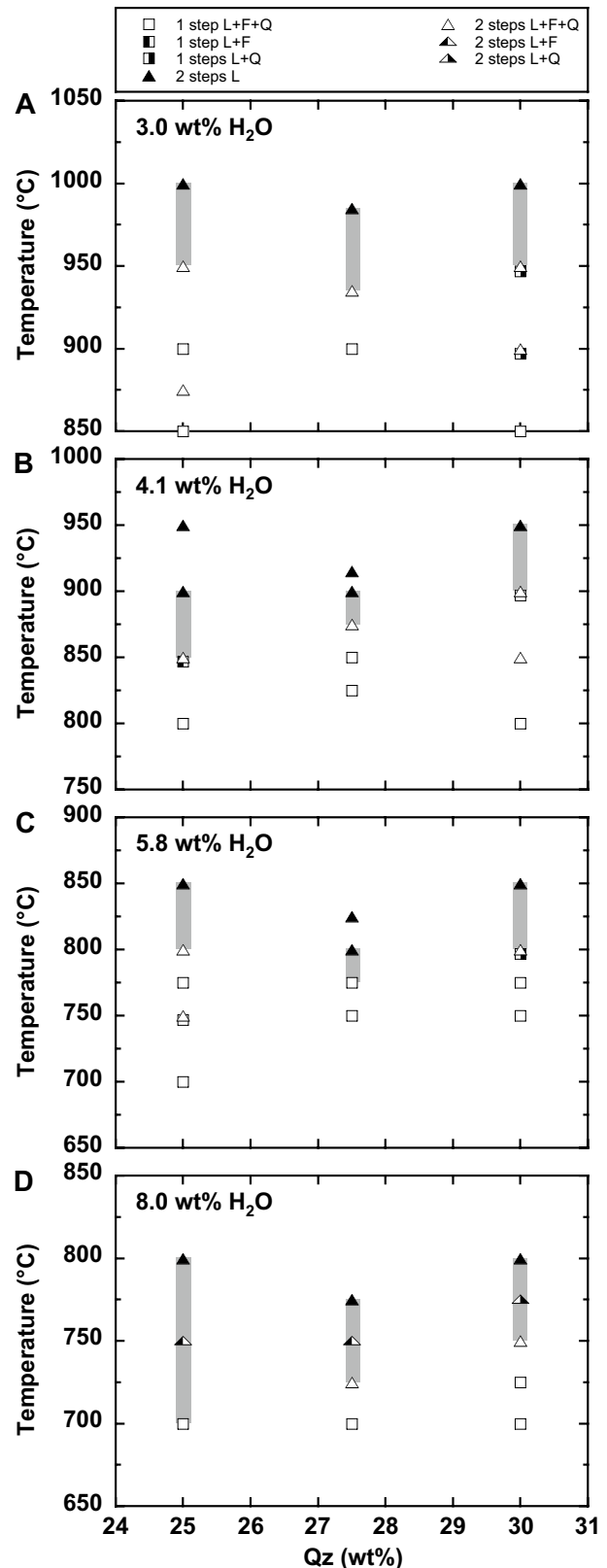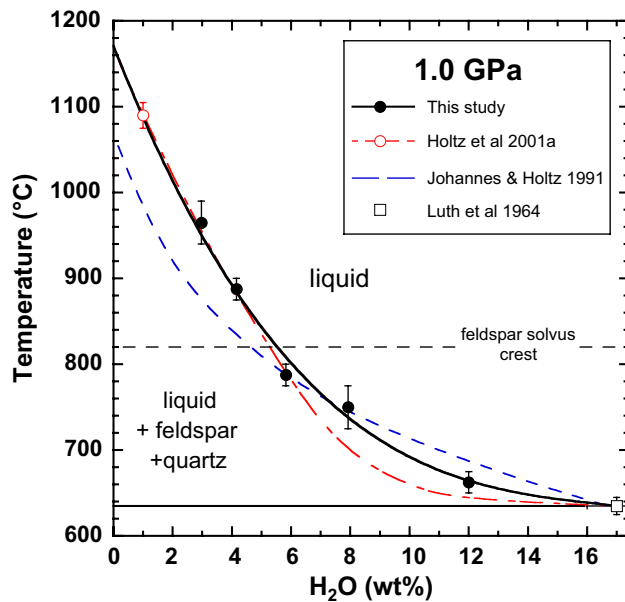
Fig. 6 Comparison of haplogranite liquidus minimum at 1.0 GPa. *Filled black circles* are bracket midpoints, this study; *error bars* denote bracket widths at 27.5 wt% Qz. *Open square* solidus at vapor saturation (Luth et al. 1964); *Open red circle* constraint at 1 wt% H_2O from Holtz et al. (2001a), extrapolated from 0.8 GPa. The *solid black curve* (Eq. 1, text) is the best fit to the bracket midpoints, the constraint from Luth et al. (1964) and Holtz et al. (2001a) (see text). Liquid taken from graphical extrapolations in Johannes and Holtz (1991) and Holtz et al. (2001a) are shown with *blue dashed* and *red dash–dot curves*, respectively

Fig. 7 $P - T$ projection of the H_2O-undersaturated haplogranite liquidus minimum. Isopleths of H_2O concentration (wt%) are constrained by this study (*filled red circles*) and previous work (*filled black circles*; Johannes 1985; Johannes and Holtz 1991; Holtz et al. 2001a, b). The H_2O-saturated solidus is based on results of Tuttle and Bowen (1958), Luth et al. (1964), Huang and Wyllie (1975), and Holtz and Johannes (1994). The H_2O isopleths based on the present work have shallower slopes than previously inferred (*dashed black lines*; Holtz et al. 2001a) at high H_2O content, though this may in part be reflective of the starting bulk composition, Or/(Ab + Or) = 0.5 (wt basis), instead of one more sodic, Or/(Ab + Or) = 0.2–0.4, which may bring the curves in closer agreement

she thought that a solid solution between sanidine and SiO_2 would be unlikely. The unit cell constants of a typical feldspar-1 formed in our experiments do not provide conclusive evidence for persiliceous sanidine, but leave open the possibility of a persiliceous precursor which recrystallized rapidly to intergrowths of feldspar + quartz.

The textures we produced are similar to those seen in natural granophyre and graphic granite and in some experiments on undercooled melts in the $KAlSi_3O_8$–SiO_2–H_2O system at 0.5 GPa (Baker and Freda 2001). Models which have been advocated emphasize coprecipitation of quartz and feldspar, resulting either from near-equilibrium cotectic growth or kinetic interface effects (Fenn 1977). In this study, we find evidence for development of these textures during replacement and reaction of an early-formed metastable feldspar, having cryptocrystalline quartz intergrowths. It seems possible that an ephemeral sanidine with excess Si_4O_8 in solid solution formed by extremely rapid cooling. The absence of the initial crystal nuclei is important, as well as rapid undercooling. Waters and Andrews (2016) found experimental and observational evidence that glassy rhyolites (obsidians) result from cooling of initially superheated H_2O-bearing magmas. The swiftly cooled debris from the Ries Kessel (Germany) impact event (Osinski 2004) and the
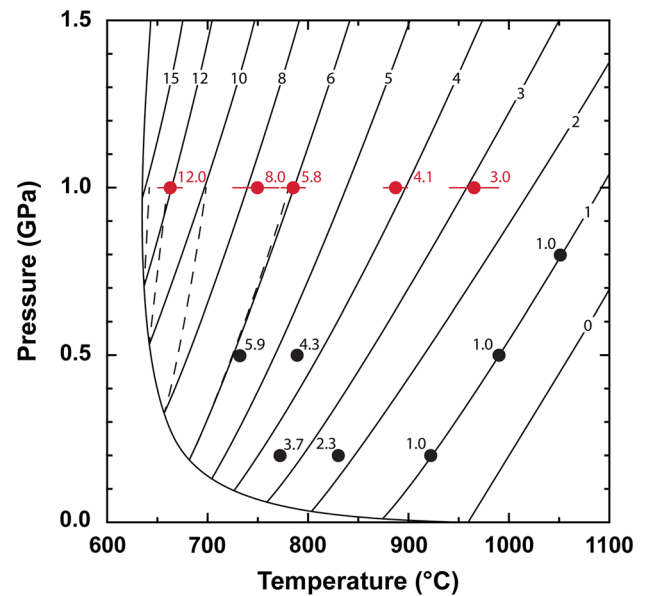
Fish Canyon (Colorado) ignimbrite deposit (Lipman et al. 1997) contain granophyre clasts having textures remarkably similar to some of those produced in the present study. It may be that H_2O content of granitic liquids, as well as supercooling, is essential for the formation of granophyre and possibly a persiliceous feldspar precursor. In any case, superheating of the precursor liquid (absence of pre-existing crystal nuclei) seems to be essential.

Some rocks from very high pressure terranes contain coesite or quartz pseudomorphs after coesite intergrown with K-feldspar (Yang et al. 1998). This may indicate that such a solid solution could exist in nature, perhaps stabilized by high pressures.

Granitic rocks and dehydration melting

Granitic rocks are diverse and they form in a variety of geologic settings. Among the important occurrences are subduction-related batholith suites such as the Sierra Nevada of California, the rhyolite–basalt bimodal volcanic "hot-spots", as in the Yellowstone area of Wyoming, and anorogenic (A-type) granites, which are widely distributed in the exposed Precambrian terranes of North America and

Eurasia. The role of H_2O in the genesis of all of these types of granitic rocks is a subject of on-going debate.

The most direct application of the present work may be to alkaline within-plate (anorogenic) granites, for several reasons. First, such granites (sensu stricto) are readily modeled by the haplogranite system. The small amounts of CaO, FeO, and MgO in typical alkaline granites are not likely to alter conclusions about the temperature dependence of H_2O content. Johannes (1984) found that at 0.2–1.5 GPa, the temperature of the haplogranite solidus rises only 3 °C if the albite component is replaced by An_{20}. Similarly, small effects are likely for FeO and MgO, which are also typically low in concentration. For example, average alkaline granite from the northern border zone of the Ketilidian mobile belt of South Greenland contains only 1.0–1.5 wt% FeO + MgO (Kalsbeek and Taylor 1985), which could not have a major effect on the H_2O content at a given temperature. In addition, the alkaline granites display higher temperature provenance than the subduction zone association (Collins et al. 2016), lower H_2O activity and conspicuous involvement of halogens, as well as high K/Na (Whaley et al. 1987). Some suites of alkaline granites, such as the Transbaikal granites of Siberia and Mongolia (Litvinovskii et al. 1994), are so abundant that they comprise nearly half of the entire continental volume in that area.

There is general agreement that these voluminous granite swarms derive mostly from melting of pre-existing intermediate-composition continental crust (Leake 1990; Wyllie et al. 1976). Large-scale melting of the crust requires both a major source of heat and, undoubtedly, a source of H_2O. The most probable source of heat for crustal melting is invasion by mantle-derived basaltic magmas (e.g., Huppert and Sparks 1988). The source rock of the within-plate granites is believed to be the intermediate tonalite-to-trondhjemite gneisses of the sort that make up the bulk of the exposed Precambrian terranes. These rocks typically contain no more than 0.6–0.8 wt% H_2O in the form of biotite and amphibole. The controversy immediately arises whether this small amount of H_2O is sufficient to yield voluminous granitic magmas by closed-system melting (dehydration melting), as advocated by many workers (Brown and Fyfe 1970; Le Breton and Thompson 1988; Brown 2001). At 1.0 GPa and 900 °C, the extrapolation of Johannes and Holtz (1991) gives 2.3 wt% as the H_2O content of granite magmas in equilibrium with alkali feldspar and quartz, as shown in Fig. 6. Johannes and Holtz (1991) point out that the granite yield at this H_2O content would be quite restricted, for temperatures which could plausibly be present over large volumes of the continental crust.

Holtz et al. (2001a) made additional measurements of granite liquidus temperatures for 1 wt% H_2O in the pressure range 0.2–0.8 GPa, and concluded that melting temperatures of haplogranites in the low-H_2O range are substantially higher than given by previous estimates. Their revision of the H_2O $P - T$ isopleths exacerbates the H_2O problem of dehydration melting, indicating that, at 900 °C and 1.0 GPa, liquidus minimum haplogranite must have 3.6 wt% H_2O. Our experiments support the higher estimate of H_2O in a granitic melt in equilibrium with feldspar and quartz, and hence, the smaller yield of granitic magma could be supplied by a deep-crustal tonalitic gneiss. According to Eq. 1, the lowest temperature at which a haplogranite melt having 4.0 wt% H_2O could exist at 1.0 GPa is 892 °C. This concentration of H_2O would require that a melt fraction no greater than 0.2 (0.8/4) could form, even in the case of complete dehydration of the residual rock. Rutter and Wyllie (1988) determined that a typical tonalite containing 0.8 wt% H_2O at 1.0 GPa would produce about 18 vol % of melt at the biotite-out point, about 900 °C. The difficulty of maintaining such high temperature over large volumes of the lower continental crust makes it seem necessary that generation of granite swarms of subcontinental dimensions like the Transbaikal granites involved input of H_2O into sites of deep-crust melting.

Several authors have suggested delivery of H_2O to sites of crustal melting, based on field studies of specific granites (summarized by Weinberg and Hasalová 2015). These mechanisms include downward circulation of surficial water in thermally driven convection cells (Wickham and Taylor 1987; McLelland et al. 2002), metasomatic alteration of the lower crust by mantle-derived fluids (Martin 2006), transfer of H_2O and other components from invading basalts into deep-crustal melts (Litvinovsky and Podladchikov 1993), and melting in the presence of concentrated brines of unknown origin (Aranovich et al. 2013).

Conclusions

- Because of severe supercooling problems, in particular delayed nucleation and the growth of metastable feldspars from supercooled granitic liquids, a reversal procedure was developed to obtain equilibrated, stoichiometric feldspars and to bracket the liquidus. Supercooling by as much as 50 °C was observed.
- Analyses of metastable feldspar produced in these experiments contain excess silica. However, unit cell refinements showed no evidence for solid solution with the monoclinic alkali feldspar structure. Longer runs and increase in temperature lead to resorption and reaction to produce a stable assemblage of either stoichiometric feldspar + quartz + liquid or at still higher two-step temperatures, liquid only. The reaction textures of feldspar–quartz intergrowths resemble some described from volcanic and impactite surge deposits.

- We present the first experimental determination of the H_2O content along the haplogranite liquidus at deep crustal P and T (625–1050 °C, 1.0 GPa). The minimum temperature of the 1.0 GPa liquidus at a given water content occurs near 27.5 wt% Qz for a composition of Or/Ab = 1 (wt%).

- Integration of the new data with previous low-pressure results yields a P–T projection of H_2O concentration in the liquid (Fig. 7). The new phase relations indicate that H_2O contents in the high-temperature range are higher than indicated by Johannes and Holtz (1991), but are in good agreement with the extrapolated values from Holtz et al. (2001a).

- Equation 1 describing the liquidus minimum can be used to make fertility calculations of the volume of magma generated by hydrous melting of deep-crustal gneisses. The high H_2O content of granites generated at the liquidus minimum at >800 °C presents a challenge for producing voluminous amounts of metaluminous granites from biotite–amphibole gneisses by dehydration melting.

References

Aranovich LY, Newton RC, Manning CE (2013) Brine-assisted anatexis: experimental melting in the system haplogranite–H_2O–NaCl–KCl at deep-crustal conditions. Earth Planet Sci Lett 374:111–120

Aranovich LY, Makhluf AR, Manning CE, Newton RC (2014) Dehydration melting and the relationship between granites and granulites. Precambr Res 253:26–37

Arzilli F, Carroll MR (2013) Crystallization kinetics of alkali feldspars in cooling and decompression-induced crystallization experiments in trachytic melt. Contrib Miner Petrol 166:1011–1027

Arzilli F, Mancini L, Voltolini M, Cicconi MR, Mohammadi S, Giuli G, Mainprice D, Paris E, Barou F, Carroll MR (2015) Near-liquidus growth of feldspar spherulites in trachytic melts: 3D morphologies and implications in crystallization mechanisms. Lithos 216:93–105

Baker DR, Freda C (2001) Eutectic crystallization in the undercooled Orthoclase-Quartz-H_2O system: experiments and simulations. Eur J Mineral 13:453–466

Bartoli O, Acosta-Vigil A, Ferrero S, Cesare B (2016) Granitoid magmas preserved as melt inclusions in high-grade metamorphic rocks. Am Min 101:1543–1559

Boettcher AL, Wyllie PJ (1968) Melting of granite with excess water to 30 kilobars pressure. J Geol 76:235–244

Brown M (2001) Orogeny, migmatites and leucogranites: a review. J Earth Sci Syst 110:313–336

Brown M (2007) Crustal melting and melt extraction, ascent and emplacement in orogens: mechanisms and consequences. J Geol Soc Lond 164:709–730

Brown GC, Fyfe WS (1970) The production of granitic melts during ultrametamorphism. Contrib Miner Petrol 28:310–318

Burnham CW, Jahns RH (1962) A method for determining the solubility of water in silicate melts. Am J Sci 260(10):721–745

Carman JH, Tuttle OF (1967) Experimental verification of solid solution of excess silica in sanidine from rhyolites. Geol Soc Am Spec Pap 115:33–34

Clemens JD, Vielzeuf D (1987) Constraints on melting and magma production in the crust. Earth Planet Sci Lett 86:287–306

Cohen LH, Klement W (1967) High-low quartz inversion: Determination to 35 kilobars. J of Geophyl Res 72:4245–4251

Collins WJ, Huang HQ, Jiang X (2016) Water-fluxed crustal melting produces Cordilleran batholiths. Geol 44:143–146

Ebadi A, Johannes W (1991) Beginning of melting and composition of first melts in the system Qz–Ab–Or–H_2O–CO_2. Contrib Mineral Petrol 106:286–295

Fenn PM (1977) The nucleation and growth of alkali feldspars from hydrous melts. Can Mineral 15:135–161

Fenn PM (1986) On the origin of graphic granite. Am Mineral 71:325–330

Grundy HD, Ito J (1974) The refinement of the crystal structure of a synthetic non-stoichiometric Sr feldspar. Am Mineral 59:1319–1326

Hayden LA, Manning CE (2011) Rutile solubility in $NaAlSi_3O_8$–H_2O fluids. Chem Geol 284:74–81

Holland TJB, Powell R (2001) Calculation of phase relations involving haplogranitic melts using an internally consistent thermodynamic dataset. J Petrol 424:673–683

Holland TJB, Redfern SAT (1997) UNITCELL: a nonlinear least-squares program for cell-parameter refinement and implementing regression and deletion diagnostics. J Appl Crystallog 30:84 (**abstract**)

Holtz F, Johannes W (1994) Maximum and minimum water contents of granitic melts: implications for chemical and physical properties of ascending magmas. Lithos 32:149–159

Holtz F, Pichavant M, Barbey P, Johannes W (1992) Effects of H_2O on liquidus phase relations in the haplogranite system at 2 and 5 kbar. Am Min 77:1223–1241

Holtz F, Becker A, Freise M, Johannes W (2001a) The water-undersaturated and dry Qz-Ab-Or system revisited. Experimental results at very low water activities and geological implications. Contribs Mineral Petrol 141:347–357

Holtz F, Johannes W, Tamic N, Behrens H (2001b) Maximum and minimum water contents of granitic melts generated in the crust: a reevaluation and implications. Lithos 56:1–14

Huang WL, Wyllie PJ (1975) Melting reactions in the system $NaAlSi_3O_8$–$KAlSi_3O_8$–SiO_2 to 35 kilobars, dry and with excess water. J Geol 83:737–748

Huppert HE, Sparks RSJ (1988) The generation of granitic magmas by intrusion of basalt into continental crust. J Petrol 29:599–624

Johannes W (1984) Beginning of melting in the granite system Qz-Or-Ab-An-H_2O. Contrib Mineral Petrol 86:264–273

Johannes W (1985) The significance of experimental studies for the formation of migmatites. In: Ashworth JR (ed) migmatites. Springer, New York, pp 36–85

Johannes W, Holtz F (1991) Formation and ascent of granitic magmas. Geol Rund 80:225–231

Johannes W, Holtz F (1996) Petrogenesis and experimental petrology of granitic rocks. Springer, Berlin, pp 19–57

Johannes J, Bell PM, Mao HK, Boettcher AL, Chipman DW, Hays JF, Nexton RC, Seifert F (1971) An interlaboratory comparison of piston cylinder pressure calibration using the albite-breakdown reaction. Contrib Mineral Petrol 32:24–38

Kalsbeek F, Taylor PN (1985) Isotopic and chemical variation in granites across a Proterozoic continental margin—the Ketilidian mobile belt of South Greenland. Earth Planet Sci Lett 73:65–80

Keppler H (1989) The influence of the fluid phase composition on the solidus temperatures in the haplogranite system

NaAlSi$_3$O$_8$–KAlSi$_3$O$_8$–SiO$_2$–H$_2$O–CO$_2$. Contrib Mineral Petrol 102:321–327

Le Breton N, Thompson AB (1988) Fluid-absent (dehydration) melting of biotite in metapelites in the early stages of crustal anatexis. Contrib Mineral Petrol 99:226–237

Leake BE (1990) Granite magmas: their sources, initiation and consequences of emplacement. J Geol Soc 147:579–589

Lipman P, Dungan M, Bachmann O (1997) Comagmatic granophyric granite in the Fish Canyon Tuff, Colorado: implications for magma-chamber processes during a large ash-flow eruption. Geology 25:915–918

Litvinovskii BA, Zanvilevich AN, Wickham SM (1994) Angara-Vitim batholith, Transbaikalia: structure, petrology, and petrogenesis. Russ Geol Geophys 35:190–203

Litvinovsky BA, Podladchikov YY (1993) Crustal anatexis during the influx of mantle volatiles. Lithos 30:93–107

London D, Morgan GB, Hervig RL (1989) Vapor-undersaturated experiments with Macusani glass + H$_2$O at 200 MPa, and the internal differentiation of granitic pegmatites. Contribs Mineral Petrol 102:1–17

Longhi J, Hayes JF (1979) Phase equilibria and solid solution along the join CaAl$_2$Si$_2$O$_8$–SiO$_2$. Am J Sci 279:876–890

Luth WC (1976) Granitic rocks. In: Bailey DK, MacDonald R (eds) The evolution of the crystalline rocks. Academic Press, London, pp 335–417

Luth WC, Jahns RH, Tuttle OF (1964) The granite system at pressures of 4 to 10 kilobars. J Geophys Res 69:759–773

Martin RF (2006) A-type granites of crustal origin ultimately result from open-system fennitization reactions in an extensional environment. Lithos 91:125–136

McLelland J, Morrison J, Selleck B, Cunningham B, Olson C, Schmidt K (2002) Hydrothermal alteration of late-to post tectonic Lyon Mountain Granitic Gneiss, Adirondack Mountains, New York: Origin of quartz–sillimanite segregations, quartz–albite lithologies, and associated Kiruna-type low-Ti Fe-oxide deposits. J Metam Geol 20:175–190

McMurdie HF, Morris MC, Evans EH, Paretzkin B, de Groot JH, Hubbard CR, Carmel SJ (1985) Standard X-ray diffraction powder patterns. US Bur Stand Monograph 25(12):1–96

Megaw HD (1970) Structural relationship between coesite and feldspar. Acta Crystallographica Section B. Struct Crystallo Cryst Chem 26:261–265

Morgan GBVI, London D (1996) Optimizing the electron microprobe analysis of hydrous alkali aluminosilicate glasses. Am Mineral 81:1176–1185

Morgan GBVI, London D (2005) Effect of current density on the electron microprobe analysis of alkali aluminosilicate glasses. Am Mineral 90:1131–1138

Morse SA (1970) Alkali feldspars with water at 5 kb pressure. J Petrol 11:221–251

Nabelek PI, Whittington AG, Sirbescu MLC (2010) The role of H$_2$O in rapid emplacement and crystallization of granite pegmatites: resolving the paradox of large crystals in highly undercooled melts. Contrib Mineral Petrol 160:313–325

Newton RC, Manning CE (2006) Solubilities of corundum, wollastonite and quartz in H$_2$O-NaCl solutions at 800 °C and 10 kbar: interaction of simple minerals with brines at high pressure and temperature. Geo Cosmo Acta 70:5571–5582

Newton RC, Manning CE (2007) Solubility of grossular, Ca$_3$Al$_2$Si$_3$O$_{12}$, in H$_2$O–NaCl solutions at 800 °C and 10 kbar, and the stability of garnet in the system CaSiO$_3$–Al$_2$O$_3$–H$_2$O–NaCl. Geo Cosmo Acta 71:5191–5202

Newton RC, Manning CE (2008) Thermodynamics of SiO$_2$–H$_2$O fluid near the upper critical end point from quartz solubility measurements at 10 kbar. Earth Planet Sci Lett 274:241–249

Orville PM (1967) Unit-cell parameters of microcline-low albite and sanidine-high albite solid solution series. Am Mineral 52:55–75

Osinski GR (2004) Impact melt rocks from the Ries structure, Germany: an origin as impact melt flows? Earth Planet Sci Lett 226:529–543

Paillat O, Elphick SC, Brown WL (1992) The solubility of water in NaAlSi$_3$O$_8$ melts: a reexamination of Ab–H$_2$O phase relationships and critical behaviour at high pressures. Contrib Mineral Petrol 112:490–500

Parsons I (1978) Alkali-feldspars: which solvus? Phys Chem Mineral 2:199–213

Perry K Jr (1968) Representation of mineral chemical analyses in 11 dimensional space. Part I. Feldspars. Lithos 1:201–218

Pichavant M (1987) Effects of B and H$_2$O on liquidus phase relations in the haplogranite system at l kbar. Am Min 72:1056–1070

Rutter MJ, Wyllie PJ (1988) Melting of vapour-absent tonalite at 10 kbar to simulate dehydration–melting in the deep crust. Nature 331:159–160

Seck HA (1971) Effect of pressure on composition of coexisting alkali feldspars and plagioclases in system NaAlSi$_3$O$_8$–KAlSi$_3$O$_8$–CaAl$_2$Si$_2$O$_8$–H$_2$O. Contrib Mineral Petrol 31:67

Sturt BA (1970) Exsolution phenomena in metamorphic minerals developed during aging with particular reference to feldspar solid solutions. Mineral Mag 37:815–832

Tropper P, Manning CE (2007) The solubility of corundum in H$_2$O at high pressure and temperature and its implications for Al mobility in the deep crust and upper mantle. Chem Geol 240:54–60

Truckenbrodt J, Johannes W (1999) H$_2$O loss during piston-cylinder experiments. Am Min 84:1333–1335

Tuttle OF, Bowen NL (1958) Origin of granite in the light of experimental studies in the system NaAlSi$_3$O$_8$–KAlSi$_3$O$_8$–SiO$_2$–H$_2$O. Geol Soc Am Memoirs 74:1–146

Waters LE, Andrews BJ (2016) The role of superheating in the formation of Glass Mountain obsidians (Long Valley, CA) inferred through crystallization of sanidine. Contribs Mineral Petrol 171:79–98

Webster JD (1997) Exsolution of magmatic volatile phases from Cl-enriched mineralizing granitic magmas and implications for ore metal transport. Geo Cosmo Acta 61:1017–1029

Weinberg RF, Hasalová P (2015) Water-fluxed melting of the continental crust: a review. Lithos 212:158–188

Whaley JB, Currie KL, Chapell BW (1987) A-type granites: geochemical characteristics, discrimination and petrogenesis. Contrib Mineral Petrol 95:407–419

Wickham SM, Taylor HP (1987) Stable isotope constraints on the origin and depth of penetration of hydrothermal fluids associated with Hercynian regional metamorphism and crustal anatexis in the Pyrenees. Contribs Mineral Petrol 95:255–268

Wright TL, Stewart DB (1968) X-ray and optical study of alkali feldspar. I. Determination of composition and structural state from refined unit-cell parameters and 2V. Am Min 53:38–87

Wyllie PJ, Huang WL, Stern CR, Maaløe S (1976) Granitic magmas: possible and impossible sources, water contents, and crystallization sequences. Can J Earth Sci 13:1007–1019

Yang J, Godard G, Smith DC (1998) K-feldspar-bearing coesite pseudomorphs in an eclogite from Lanshantou (Eastern China). Euro J Mineral 10:969–986